

CRISTAL: Real-time Camera Registration in Static LiDAR Scans using Neural Rendering

Joni Vanherck Steven Moonen Brent Zoomers Kobe Werner
 Jeroen Put Lode Jorissen Nick Michiels
 Hasselt University - Digital Future Lab - Flanders Make
 {firstname}.{lastname}@uhasselt.be

Abstract

Accurate camera localization is crucial for robotics and Extended Reality (XR), enabling reliable navigation and alignment of virtual and real content. Existing visual methods often suffer from drift, scale ambiguity, and depend on fiducials or loop closure. This work introduces a real-time method for localizing a camera within a pre-captured, highly accurate colored LiDAR point cloud. By rendering synthetic views from this cloud, 2D–3D correspondences are established between live frames and the point cloud. A neural rendering technique narrows the domain gap between synthetic and real images, reducing occlusion and background artifacts to improve feature matching. The result is drift-free camera tracking with correct metric scale in the global LiDAR coordinate system. Two real-time variants are presented: Online Render & Match and Prebuild & Localize. We demonstrate improved results on the ScanNet++ dataset and outperform existing SLAM pipelines.

1. Introduction

Accurate, real-time camera localization is essential for robotics and Extended Reality (XR), enabling reliable navigation and immersive experiences. A robust, drift-free global pose allows autonomous robots to orient instantly and XR devices to consistently align digital twins with the real world. Existing methods still face several key challenges. They accumulate drift over time, leading to inaccuracies. They often rely on artificial landmarks (e.g., fiducial markers [9]), requiring modifications to the environment and causing visual distractions, which is not always allowed in industrial cases. In addition, monocular tracking leaves scale ambiguity unresolved. Especially for monocular systems in large areas, drift is a severe problem. Even in a relatively small area of 6×4 meters, state-of-the-art XR headsets, with multiple cameras and IMU sensor integrated, experience tracking errors of several centimeters due to drift

accumulation as shown by Singh *et al.* [32]. Loop closing [22] solves this issue to some extent: it can reduce drift by recognizing previously explored areas and updating the map accordingly. However, creating a well-covered SLAM map with loop closing takes time and causes pose jumps when optimizing the map. Loop closure may fail in low-overlap areas such as hallways, where drift can still accumulate.

Static LiDAR mapping provides dense 3D point clouds with highly accurate distance measurements and an absolute scale, making it well suited for large-scale scene reconstruction. Combining LiDAR with visual sensors thus offers many opportunities for improving image localization and camera tracking. Although static LiDAR scanners are expensive, our method requires a single complete, high-quality scan to create the global tracking map. Since the scan only needs to be captured once, renting a scanner or outsourcing acquisition is feasible. A static LiDAR scan also defines a single global coordinate system, facilitating content authoring for a digital twin.

Some methods use simultaneously captured image–LiDAR data [13, 41], but they rely on accurate extrinsic calibration, precise time synchronization, and costly hardware. In many cases, onboard LiDAR is impractical due to added size, weight, and system complexity.

We present a method for real-time camera localization within a pre-captured, high-accuracy colored LiDAR point cloud. Our approach generates synthetic images from LiDAR scans to establish 2D–3D correspondences between live camera frames and the point cloud in real time. A key barrier lies in the domain gap between synthetic renders and real images: point cloud renders often suffer from holes due to occlusions and limited point cloud density, or artifacts such as background information leaking into the foreground, both of which interfere with reliable feature extraction. To address this, we adapt a neural rendering technique [5, 6, 11, 26, 35], which mitigates these artifacts and narrows the domain gap, thereby improving feature detection and matching. This enables us to exploit the metric

accuracy of LiDAR while retaining the flexibility of image-based tracking. In particular, our method provides drift-free localization, correct metric scale from the beginning, and consistent tracking within a single global coordinate system (from the LiDAR point cloud). Additionally, synthetic rendering allows us to vary lighting conditions and contrast, which may further increase the robustness of our approach.

Concretely, our contributions are:

- **2D-3D matching between images and point clouds:** We improve 2D-3D matching capabilities between LiDAR point clouds and images using a real-time neural renderer. We introduce two methods for camera localization:
 - **Online Render & Match method (R&M):** A method to localize a camera in a LiDAR point cloud with very little manual work or preprocessing. We do this by rendering synthetic images from the point cloud and matching them with real camera images.
 - **Prebuild & Localize (P&L):** A method to create a feature map from synthetic point cloud renders, so they can be used with traditional, real-time SLAM methods for localization, with almost no manual work.
- **Ground-truth datasets:** We build a ground-truth dataset for camera localization in a colored LiDAR point cloud using a sub-millimeter accurate motion capture system. We also created a synthetic dataset for ground-truth evaluation by simulating a LiDAR scanner in Unity.

2. Related work

Image-to-point cloud registration is a well-studied topic, with varying methods to solve this problem. For instance, Colmap-PCD [1] tries to localize images in a non-colored point cloud with plane features. Similarly, Scannet++ [39] renders images from an RGB laser scan and includes them in the COLMAP [30] pipeline. They refine the poses with dense photometric error guided by the laser scan. This simplifies the 2D-3D matching problem to a 2D-2D matching problem, relying on well-established detect-and-match pipelines. These methods require a significant amount of processing time and only process a subset of the frames, making them unsuitable for real-time tracking solutions.

Early camera localization methods within pre-captured LiDAR maps include Caselitz *et al.* [2] and Kim *et al.* [12]. Both methods exploit point cloud geometry, which is more robust to lighting changes, but makes them incapable of distinguishing geometrically similar structures. The latter requires the use of stereo cameras. Caselitz *et al.* [2] do not perform direct localization within the point cloud. Instead, they build a local map via Visual Odometry (VO) and align it with the LiDAR map. This local reconstruction is susceptible to noise and drift, making the VO–LiDAR alignment harder and dependent on VO accuracy. Their method also requires an initial alignment estimate.

Yu *et al.* [40] propose a method that uses visual-inertial

odometry (VIO) to predict the camera pose and establish correspondences between 2D image lines and 3D lines. A drawback of this approach is its reliance on VIO: if the odometry drifts or the overlap between views is too small, the method cannot find sufficient correspondences, and pose optimization fails. They also require a manual initial pose.

More recently, neural methods [3, 4, 15, 27] such as CMRNet [3] and CMRNet++ [4] use a CNN to align a projected LiDAR depth map with an RGB color image. However, they require a rough estimate of the camera pose, and do not generalize well to unseen scenes. Additionally, these neural methods are trained with a maximum translation of up to 10 meters, making them unsuitable for direct, global image-to-point cloud registration.

Other methods find 2D–3D correspondences between images and point clouds and use PnP [14] to estimate the relative pose. 2D3D-MatchNet [7], LCD [24], and P2-Net [36] extract image features (*e.g.* SIFT [18]) and point cloud features (*e.g.* ISS [43]) to learn intermodal descriptors for matching. However, these methods face a large domain gap: image features rely on texture and color, while 3D features depend on local geometry. This makes repeatable key-points and descriptors difficult to compute, resulting in few inlier matches. Neural intermodality matching methods, such as 2D3D-MaTR [16], Diff²I2P [21], and FreeReg [37], use transformers [16] and diffusion priors [21, 37] to match image and point cloud features, but they are computationally heavy and generalize poorly to unseen scenes compared to intra-modal matching.

Most prior work has focused on non-colored point clouds. In many cases, however, a colored point cloud is available, for example from a static LiDAR scanner, providing more information about the environment to be exploited. Munoz-Salinas *et al.* [23] project colored point clouds onto images and localize using feature-based matching. Their approach, however, requires either an initial known pose or a rough trajectory. In addition, they rely on point-based rendering, which struggles with sparse point clouds or scans that include significant background leakage. They also experiment with a neural rendering approach [17], but this requires an extensive preprocessing and already-registered camera poses, which is the problem being solved. In contrast, our method employs a neural rendering approach that requires neither preprocessing nor prior camera poses and operates without an initial trajectory. Michiels *et al.* [19] localize a camera within a point cloud by building a SLAM map and undistorting it using markers detected in both the point cloud and camera frames. They further refine the map by matching video frames and point cloud renders with known poses. Their method requires marker placement and extensive preprocessing, and relies on a point-based renderer. Moreover, it corrects drift after it occurs, while our approach prevents drift accumulation entirely.

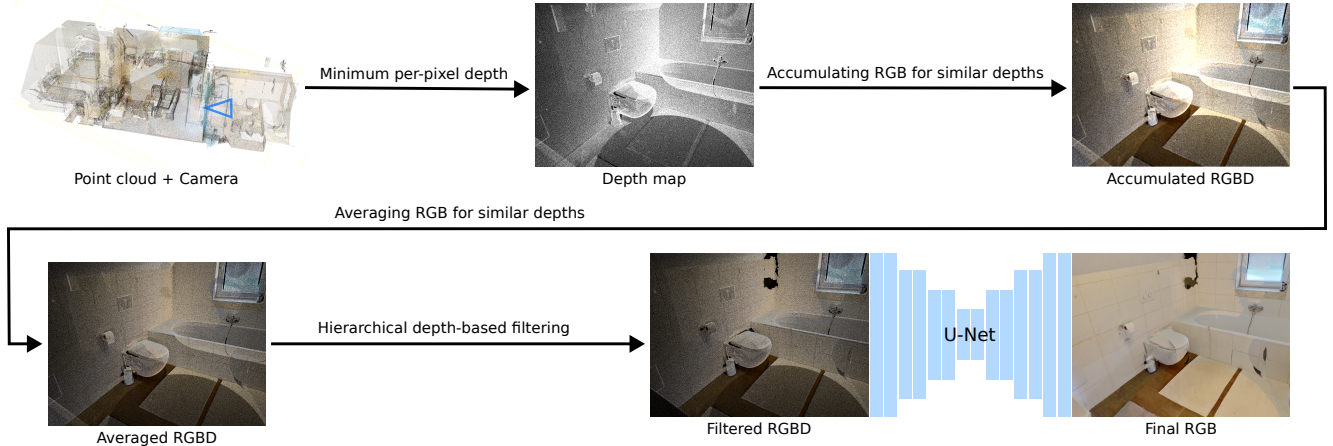


Figure 1. Overview of the adapted neural renderer. First, the per-pixel minimum depth is computed using z-buffering. In the second pass, colors of points projecting to the same pixel and within a small depth threshold are accumulated and then averaged. Remaining background leakage is removed via a hierarchical depth filter, and holes are filled using a U-Net.

3. Methodology

We propose two methods for camera localization with respect to a point cloud: (1) Online Render & Match (R&M) and (2) Prebuild & Localize (P&L). The first method uses real-time neural rendering to synthesize a virtual image from the last known pose, which is then matched with the next camera frame. While R&M requires real-time GPU rendering, our second method, P&L, precomputes a SLAM map offline, enabling efficient, real-time tracking using standard SLAM pipelines. Both approaches rely on a neural renderer for high-fidelity LiDAR point clouds, inspired by Vanherck *et al.* [35]. The renderer projects 3D points into a 2D image plane using a hierarchical depth filter to remove background points leaking into the foreground, and employs a U-Net [28] to fill gaps in the image. An overview of the neural rendering pipeline is shown in Fig. 1. Our methods do not require any scene-specific training or tuning and achieve real-time performance on commodity hardware.

3.1. Neural Point Cloud Renderer

Let the LiDAR point cloud be $P = (X_i, C_i)$ where $X_i \in \mathbb{R}^3$ are 3D points and $C_i \in \mathbb{R}^3$ their RGB colors. Given a camera pose $T_c = [R|t] \in SE(3)$ and intrinsic matrix K , each point is projected to the image plane as

$$p_i = \pi(K(RX_i + t)), \quad (1)$$

where π denotes perspective division.

Rather than relying on frustum culling and thread locking to handle cases where multiple points project to the same pixel, we divide the point cloud projection into three passes, as outlined by Schütz *et al.* [31]:

1. Depth pass: compute per-pixel minimum depth $z_{min}(p)$ using z-buffering.
2. Color accumulation: retain points within a threshold δ of $z_{min}(p)$.
3. Averaging: compute per-pixel color as

$$I(p) = \frac{1}{|\mathcal{N}(p)|} \sum_{X_i \in \mathcal{N}(p)} C_i, \quad (2)$$

where $\mathcal{N}(p)$ is the set of points that project to pixel p and are close to the nearest depth (within threshold δ).

Background leakage is then removed by a hierarchical depth filter [35], followed by a U-Net hole-filling network \mathcal{U} :

$$I_{clean} = \mathcal{U}(\text{DepthFilter}(I)) \quad (3)$$

We adopt the same U-Net configuration as Vanherck *et al.* [35], compiled using NVIDIA TensorRT for improved inference efficiency.

The neural point cloud renderer outputs a hole-filled RGB image and a background-filtered depth map from a given point cloud, using the camera’s extrinsic and intrinsic parameters:

$$(I_c^{\text{synth}}, D_c^{\text{synth}}) = \mathcal{R}(P, T_c, K_c). \quad (4)$$

Compared to Vanherck *et al.*, this design eliminates the frustum-culling overhead and synchronization locks, resulting in a $\sim 1.75\times$ speedup with identical visual quality for a resolution of 960×720 and a point cloud of 58M points. For the same resolution and a point cloud of 288M, our design speeds up the rendering process 32 times.

3.2. Online Render & Match

The online Render & Match method performs absolute camera localization by matching the live camera feed to

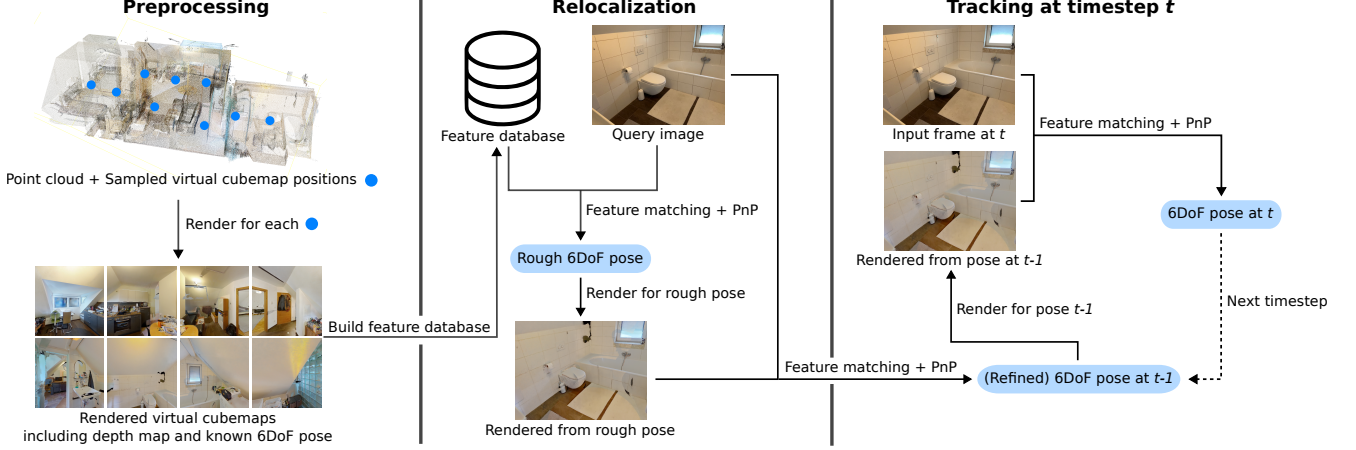


Figure 2. Overview of the proposed online Render & Match (R&M) pipeline. **Preprocessing:** synthetic cubemap images and depth maps are rendered from uniformly sampled poses within the LiDAR point cloud, using the neural rendering method described in Sec. 3.1. Features are extracted and back-projected to their 3D coordinates, forming a map database that links 2D descriptors to ground-truth 3D landmarks. **Relocalization:** when no prior pose is available, query image features are matched to the database to obtain a coarse 6DoF pose via PnP, which is refined by re-rendering the point cloud at the estimated pose. **Tracking:** during tracking, the previous pose is used to render a synthetic view, which is matched to the live camera frame to estimate the current 6DoF pose. Both stages operate without drift since all correspondences are derived from the LiDAR-based ground-truth geometry.

synthetic views of the point cloud, generated by the neural rendering method outlined in Sec. 3.1. Since each synthetic view has a known ground-truth pose and depth from the LiDAR scan, we can establish 2D-3D correspondences directly without temporal drift. An overview is given in Fig. 2. For feature extraction and matching in this pipeline, we choose XFeat [25] because the deep neural features are more robust to viewpoint and lighting changes compared to ORB [29], while achieving real-time performance with GPU inference.

Relocalization To enable camera relocalization within the point cloud, we precompute a database of synthetic keyframes. We designed a lightweight GUI tool that allows the user to define a region of interest within the point cloud, from which 3D positions are uniformly sampled to serve as virtual keyframe locations. This is the only manual step required in the preprocessing stage. For each uniformly sampled 3D pose $T_j \in SE(3)$ within the point cloud, we render a cubemap with a depth map $(I_j, D_j) = \mathcal{R}(P, T_j, K_{\text{cubemap}})$ using the neural renderer, where K_{cubemap} is the camera matrix used to generate a cubemap image. We use cubemaps to maximize coverage in each direction. From each view we extract a set of features using XFeat: $\mathcal{F}_j = \{(d_{jk}, X_{jk})\}_{k=1}^{N_j}$, where d_{jk} denotes the XFeat descriptor and X_{jk} the corresponding 3D point obtained by back-projecting pixel coordinates (u_{jk}, v_{jk}) using depth map D_j :

$$X_{jk} = T_j \cdot D_j^{\text{synth}}(u_{jk}, v_{jk}) \cdot K_{\text{cubemap}}^{-1} \cdot \begin{bmatrix} u_{jk} \\ v_{jk} \\ 1 \end{bmatrix}. \quad (5)$$

These sets of descriptors and corresponding 3D points are stored in the feature database \mathcal{D} . At runtime, features $\{d_i^q\}$ extracted from the query image I_q are matched against descriptors in \mathcal{D} . When sufficient matches $\{m_i^q\} = \{(u_i^q, v_i^q)\}$ are found for a keyframe, the resulting correspondences $\{(m_i^q, X_i)\}$ are used to estimate a rough camera pose $T_{qr} = \text{PnP}_{\text{RANSAC}}(\{m_i^q\}, \{X_i\}, K_c)$ [8, 14]. This coarse pose is then refined by re-rendering the point cloud for T_{qr} and re-estimating feature correspondences, yielding the refined pose T_q , which serves as the initialization for the tracking stage. The choice of XFeat is crucial for relocalization. Its robustness to viewpoint changes and varying intrinsic parameters (cubemap vs. camera image) reduces the number of required cubemaps compared to methods such as ORB [29], and enables tracking to be camera-agnostic. Relocalization runs in real time on the scenes we tested. However, to improve efficiency and scalability to larger environments, Bag-of-Words techniques [22] could be explored.

Tracking Given a camera image I_t at timestep t , the camera matrix K_c and the last computed 6DOF pose T_{t-1} :

1. Render the point cloud P from T_{t-1} to obtain a synthetic view and depth: $(I_{t-1}^{\text{synth}}, D_{t-1}^{\text{synth}}) = \mathcal{R}(P, T_{t-1}, K_c)$.
2. Extract features using XFeat [25] in both I_t and I_{t-1}^{synth} .
3. Match 2D features between the camera image and the synthetic view. Denote each match as a pair of pixel coordinates $m_k = ((u_k^t, v_k^t), (u_k^s, v_k^s))$, where (u_k^t, v_k^t) is the pixel in the camera image I_t and (u_k^s, v_k^s) is the corresponding pixel in the synthetic image I_{t-1}^{synth} .
4. For each match, back-project the synthetic pixel (u_k^s, v_k^s) using the synthetic depth to obtain the 3D landmark X_k .

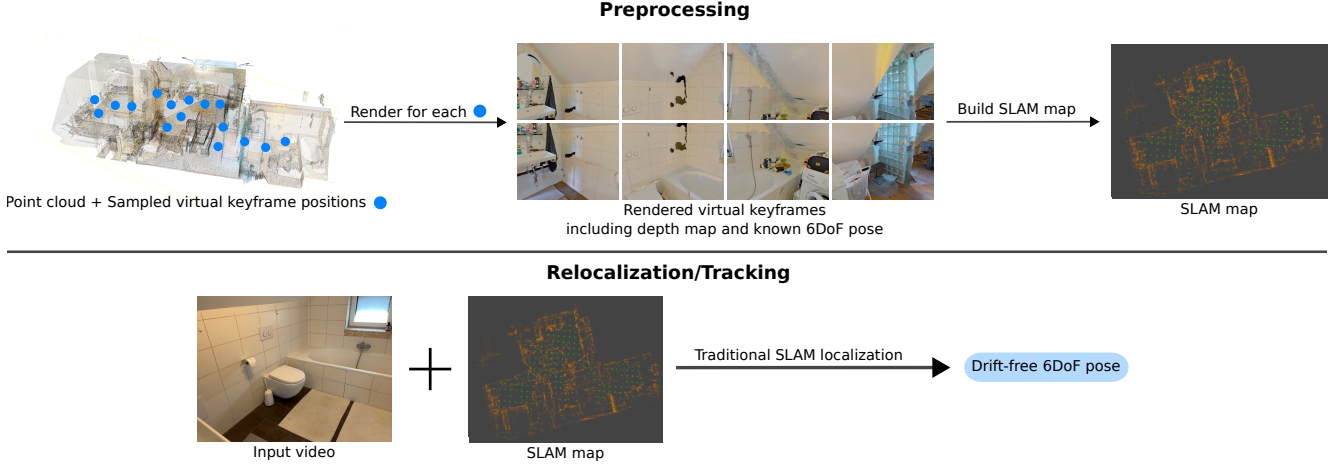


Figure 3. Overview of the proposed Prebuild & Localize (P&L) pipeline. **Preprocessing:** We generate a set of rendered keyframes and landmarks directly from the LiDAR point cloud, resulting in a compact and drift-free SLAM map created entirely offline. **Relocalization/Tracking:** the SLAM backend operates on this prebuilt map without modification, enabling real-time, drift-free 6DoF tracking.

(in world coordinates):

$$X_k = T_{t-1} \left(D_{t-1}^{\text{synth}}(u_k^s, v_k^s) \cdot K_c^{-1} \begin{bmatrix} u_k^s \\ v_k^s \\ 1 \end{bmatrix} \right). \quad (6)$$

5. Estimate the 6DOF pose with PnP-RANSAC [8, 14] using the matches in the camera image $\{(u_k^t, v_k^t)\}$ and their corresponding 3D landmarks $\{X_k\}$:

$$T_t = \text{PnP}_{\text{RANSAC}}(\{(u_k^t, v_k^t)\}, \{X_k\}, K_c). \quad (7)$$

6. Next timestep: $T_{t-1} \leftarrow T_t$.

Using this approach, there is no accumulation of drift, since each measurement stems from an accurately pre-captured LiDAR point cloud. The next section introduces a method that requires neural rendering only during preprocessing, making it more efficient and able to run on hardware without a powerful GPU.

3.3. Prebuild & Localize

For this approach, instead of Simultaneous Localization And Mapping (SLAM), we split the process in two separate stages: mapping and localization. For mapping, we propose to create a map directly from the LiDAR point cloud. Our proposed method is displayed in Fig. 3. We take a similar approach as in Sec. 3.2 to achieve this. Again, we sample 3D positions on a uniform grid within the point cloud. We render cubemap-like images/keyframes using the intrinsic properties of the camera $(I_j, D_j) = \mathcal{R}(P, T_j, K_{\text{cam}})$. To enhance vertical coverage, we render two views per direction, one slightly pitched upward and one downward. From each rendered image, we extract ORB features and associate them with their corresponding 3D landmarks:

$\mathcal{F}_j = \{(d_{jk}, X_{jk})\}_{k=1}^{N_j}$ where d_{jk} denotes the ORB descriptor and X_{jk} the reconstructed 3D landmark, analogous to Eq. (5). For SLAM map creation, landmarks observed in multiple keyframes should correspond to a single map point. For each keyframe, all landmarks are projected to the image plane using Eq. (1). Feature correspondences are sought within a small 3×3 pixel window around each keypoint, making matching efficient while filtering noisy LiDAR measurements. Matching landmarks are then merged and the map database is updated accordingly. Landmarks observed by only a single keyframe are removed from the map, as they contribute little to tracking while unnecessarily increasing map density. We generate the map in OpenVSLAM’s [33] format to ensure compatibility with its SLAM implementation. The resulting SLAM map is drift-free, as each keyframe and landmark is positioned using ground-truth poses obtained directly from the laser scan. While our approach can be applied to other visual SLAM frameworks, these were not implemented in this work. In Sec. 4, we show this approach improves localization accuracy compared to traditional SLAM.

During localization, the SLAM backend operates unmodified with the prebuilt map. This design eliminates the need for online rendering, resulting in significantly lower computational load while maintaining real-time, drift-free localization. The only preprocessing cost lies in the one-time offline generation of the SLAM map. The existing SLAM pipeline can also be leveraged to keep the map up to date with changes in the environment.

4. Evaluation

In this section, we evaluate the performance of our localization methods. We conduct experiments on both a

large-scale public dataset, ScanNet++ [39], and two custom datasets. Our evaluation focuses on the robustness and accuracy of camera registration, and runtime performance. Lastly, an ablation study is done on our custom dataset, providing insights on the impact of the neural renderer compared to plain point-based rendering. All experiments were performed on a laptop equipped with an Intel i7-13850HX CPU and an RTX 3500 Ada GPU. We use OpenVSLAM’s [33] format for both map creation and localization. Accordingly, our method is compared against the standard OpenVSLAM implementation. Throughout the rest of this paper, the term SLAM refers specifically to OpenVSLAM’s implementation.

4.1. ScanNet++ Evaluation

We evaluate our method on the ScanNet++ [39] dataset, which provides dense LiDAR point clouds with registered camera images. Camera poses in ScanNet++ were obtained by running a standard COLMAP [30] pipeline and supplementing it with rendered pseudo-images from the point cloud. By registering the renders with the camera images, scale can be recovered. These poses are further refined by minimizing a dense photometric error guided by the LiDAR geometry. It should be noted, however, that these poses are not perfect and should be considered as approximate references rather than ground truth.

We evaluate 12 scenes from the dataset. Due to computational constraints, ScanNet++ attempts to localize only every 10th frame, and not all of these attempts succeed. In contrast, our method performs online localization on every frame in the video stream, demonstrating its efficiency and robustness. The quantitative results are summarized in Tab. 1. For ScanNet++ we report the number of frames for which a pose is provided in the dataset, while for our methods we report two quantities: (1) the total number of frames successfully localized, and (2) the number of successfully localized frames out of the frames attempted by ScanNet++ (every 10th frame). We further compute translational and rotational differences between our estimated poses and those provided by ScanNet++, which indicate local consistency but not absolute accuracy, since the ScanNet++ poses are only approximate. To quantitatively assess camera-to-point-cloud alignment, we also report the Structural Similarity Index Measure (SSIM) [38] between the query image and its corresponding LiDAR render. SSIM is used because it captures structural differences and is less sensitive to color changes. We do not use other image-based metrics, such as Peak Signal-to-Noise Ratio (PSNR), because the domain gap between RGB images and LiDAR-based renders makes them less meaningful.

The results show that the R&M variant is more robust, successfully localizing more images than both ScanNet++ and our P&L poses. In contrast, the P&L variant achieves

the highest SSIM scores, indicating better photometric alignment, thanks to landmark filtering during map creation and the built-in pose optimization frameworks. Figure 4 illustrates several examples of rendered views overlaid with real camera images, where visible ghosting or blur indicates pose misalignment.

Table 1. Average localization metrics for each method across all scenes. The ‘#Frames’ column shows the *total number of frames estimated / number of frames estimated from ScanNet++ attempts*. ‘Pos./Ang.’ reports translation/rotation error relative to the estimated ScanNet++ poses. ScanNet++ does not report these errors, as it is compared against the R&M and P&L methods. The best values are highlighted in bold.

Method	#Frames	Pos./Ang. (m/°)	SSIM ↑
ScanNet++	- / 1043	- / -	0.667
R&M _{ours}	11485 / 1148	0.033 / 0.964	0.687
P&L _{ours}	8362 / 836	0.027 / 0.662	0.696

Table 2. Absolute Pose Error (APE) RMSE for each sequence and method on our custom datasets. ‘Pos.’ and ‘Ang.’ report the positional (m) and angular (°) RMSE with respect to the ground-truth measurements. The ‘#Frames’ column shows the number of frames successfully estimated by each method. SLAM denotes the default OpenVSLAM method. Best values per sequence are highlighted in bold.

Seq.	Method	#Frames	Pos. [m]	Ang. [°]
lab_1	SLAM	4381	0.084	1.338
	R&M _{ours}	4444	0.014	0.823
	P&L _{ours}	4444	0.013	0.825
lab_2	SLAM	4299	0.007	0.569
	R&M _{ours}	4299	0.008	0.568
	P&L _{ours}	4296	0.005	0.569
lab_3	SLAM	4168	0.012	0.543
	R&M _{ours}	4172	0.009	0.531
	P&L _{ours}	4172	0.006	0.539
synth_1	SLAM	2075	0.132	0.381
	R&M _{ours}	2075	0.025	0.103
	P&L _{ours}	2071	0.019	0.072
synth_2	SLAM	1899	0.486	1.452
	R&M _{ours}	1899	0.024	0.110
	P&L _{ours}	1870	0.017	0.082
synth_3	SLAM	1243	0.155	0.502
	R&M _{ours}	1585	0.031	0.136
	P&L _{ours}	1585	0.023	0.085



Figure 4. Each image displays an overlay of the target camera frame and a neural rendering of the point cloud generated from the estimated camera pose. We show results for ScanNet++, the Render & Match approach, and the Prebuild & Localize method. Misalignment, visible as ghosting or blur, suggests pose estimation errors.

4.2. Custom Dataset Evaluation

For quantitative evaluation, we created two ground-truth datasets:

- **Lab dataset:** a real-world dataset using a sub-millimeter accurate motion capture system and a Leica RTC360 scanner, capturing an area of $\sim 6 \times 6$ m,
- **Synthetic dataset:** a dataset simulating a static LiDAR scanner in Unity, covering $\sim 60 \times 40$ m.

More information about the acquisition of these datasets can be found in the supplementary material Sec. 6. These datasets allow an evaluation of our system’s accuracy and its ability to mitigate drift.

Table 2 presents the accuracy comparison between standard SLAM, the P&L method, and the R&M method. The table reports both positional and angular accuracy, as well as the number of successfully tracked frames in each sequence. For the SLAM baseline in the lab dataset, a map was generated using the *lab_2* sequence, as it was recorded with the slowest motion and thus lowest amount of motion blur. This map was then used to localize all three sequences. For the synthetic dataset, we ran each SLAM sequence

twice, once for building a map with loop closure, and once for the actual tracking. We apply Sim(3) Umeyama alignment [10, 34] to match SLAM’s trajectory with the ground-truth trajectory, and SE(3) Umeyama alignment [10, 34] for our methods, since our approaches already operate at the correct scale while SLAM uses an arbitrary scale.

As seen in the results, our methods outperform standard SLAM in accuracy while maintaining robustness, showing that neural rendering effectively bridges the gap between synthetic and real views. For sequence *lab_1* and the synthetic sequences, accuracy decreases due to rapid movements and motion blur. However, our methods still outperform the standard SLAM significantly.

To evaluate the impact of neural rendering compared to plain point-based rendering, we conducted experiments with neural rendering both enabled and disabled for several point cloud decimations. Background leakage is minimal in this single-room scan, which might favor the method without neural rendering. The original point cloud contains 71M points. Results are presented in Tab. 3. We also report the frames per second (FPS) and the preprocessing time required to build a map or feature database.

Table 3. Comparison of our methods with neural and point-based rendering variants (neural/point-based) across different decimation levels on the lab dataset. ‘Pos.’ and ‘Ang.’ report the positional (m) and angular (°) RMSE with respect to the ground truth. ‘Preproc’ shows preprocessing time in seconds. The ‘#Frames’ column shows the number of frames successfully estimated by each method. Best values are highlighted in bold. The number of keyframes and landmarks in each SLAM map are also reported.

Render & Match <small>ours</small>							
Dec.	Pos. [m]	Ang. [°]	FPS	Preproc [s]	#Frames		
100%	0.010 / 0.021	0.641 / 1.027	13.0 / 18.7	4.59 / 1.43	4305 / 4305		
75%	0.010 / 0.025	0.641 / 0.820	13.3 / 16.3	4.06 / 1.29	4305 / 4270		
50%	0.011 / 0.039	0.643 / 0.903	13.3 / 13.3	3.96 / 1.13	4305 / 4202		
33%	0.011 / 0.154	0.645 / 7.655	13.3 / 11.7	4.31 / 1.14	4305 / 3877		
20%	0.011 / 0.146	0.647 / 15.053	13.3 / 12.0	3.83 / 1.14	4305 / 2261		
10%	0.012 / 0.268	0.650 / 24.297	13.3 / 16.7	4.23 / 1.02	4305 / 210		

Prebuild & Localize <small>ours</small>							
Dec.	Pos. [m]	Ang. [°]	FPS	Preproc [s]	#Frames	#Keyframes	#Landmarks
100%	0.008 / 0.114	0.644 / 4.645	20.7 / 15.0	144.78 / 419.69	4304 / 4298	594 / 608	88011 / 219001
75%	0.008 / 0.261	0.644 / 7.800	21.7 / 14.0	129.02 / 505.86	4304 / 3553	579 / 624	76551 / 199483
50%	0.008 / 0.373	0.644 / 8.683	22.7 / 12.7	127.48 / 651.88	4290 / 2217	622 / 680	64484 / 195577
33%	0.009 / 0.457	0.643 / 19.621	24.7 / 15.7	87.78 / 597.70	4287 / 2921	548 / 632	42606 / 166973
20%	0.011 / 0.603	0.687 / 12.575	26.3 / 15.0	73.39 / 605.95	4206 / 2040	530 / 624	27421 / 147284
10%	0.015 / 0.409	0.748 / 45.954	30.3 / 15.0	43.94 / 755.57	3222 / 705	409 / 696	9549 / 151057

As shown in both tables, neural rendering consistently outperforms point-based rendering across all metrics. It maintains higher accuracy and robustness while downsampling the point cloud. For the P&L method, a lower point cloud density also improves speed and efficiency when using neural rendering. In contrast, point-based rendering produces many empty pixels, which often trigger false detections from feature extractors. The resulting descriptors tend to be similar due to missing pixels, leading to a larger number of incorrectly matched features and, consequently, more landmarks in the map. These mismatches increase preprocessing time, due to more features to process, and reduce FPS due to more landmarks to match and slower RANSAC convergence. For the Render & Match method, preprocessing time with point-based rendering is lower because there is no neural rendering overhead and features are only extracted and stored without further processing. However, FPS behavior is more nuanced: with point-based rendering, ill-matched features caused by empty pixels make it harder for RANSAC to converge quickly, reducing efficiency. With a higher point cloud density this is less of a concern, because features can still be detected reliably. Also, when comparing the Prebuild & Localize and Render & Match methods, we observe that Render & Match is more robust, successfully localizing every frame in all sequences across all decimation levels, though with a reduction in FPS compared to Prebuild & Localize. Pose estimates remain accurate for both methods, even when retaining only 10% of the point cloud.

5. Conclusion & Future Work

We present a novel method for 2D–3D matching between images and LiDAR point clouds, leveraging neural rendering to bridge the domain gap between synthetic renders and real camera images. Two approaches are introduced to achieve camera registration within the LiDAR point cloud: (1) Online Render & Match, and (2) Prebuild & Localize. Our methods were evaluated on the ScanNet++ dataset and two custom ground-truth datasets. Experimental results demonstrate that our approaches improve camera pose estimation compared to ScanNet++ and standard SLAM, achieving accurate pose estimates directly within an up-to-scale global coordinate system in real-time. Our Prebuild & Localize method constructs a drift-free SLAM map offline, which can be used by traditional SLAM pipelines without modification. It is compatible with any visual map-based SLAM pipeline. Our work is a step toward practical AR applications, enabling easy content authoring and visualization in a global reference frame.

Several directions are promising for future work. First, varying the lighting conditions of synthetic renders could further enhance the robustness of 2D–3D matching. Second, our current method relies on a pre-acquired LiDAR scan of the environment, which may limit tracking if the environment undergoes significant changes. A potential solution is dynamic map updating: fixed LiDAR-based landmarks could maintain stability, while new features are added online by a mapping module to account for environmental changes.

Acknowledgements

This research was funded by the Special Research Fund (BOF) of Hasselt University (R-14360) and FWO fellowship grants (1S80926N, 1SHDZ24N), the Flanders Make's ALARMM SBO project (R-15482), and the Flanders Make's XRTWin SBO project (R-12528). This work was made possible with the support of MAXVR-INFRA, a scalable and flexible infrastructure that facilitates the transition to digital-physical work environments.

References

- [1] Chunge Bai, Ruijie Fu, and Xiang Gao. Colmap-PCD: An Open-source Tool for Fine Image-to-point cloud Registration. In *2024 IEEE International Conference on Robotics and Automation (ICRA)*, pages 1723–1729, 2024. 2
- [2] Tim Caselitz, Bastian Steder, Michael Ruhnke, and Wolfram Burgard. Monocular camera localization in 3D LiDAR maps. In *2016 IEEE/RSJ International Conference on Intelligent Robots and Systems (IROS)*, pages 1926–1931, 2016. ISSN: 2153-0866. 2
- [3] D. Cattaneo, M. Vaghi, A. L. Ballardini, S. Fontana, D. G. Sorrenti, and W. Burgard. CMRNet: Camera to LiDAR-Map Registration. In *2019 IEEE Intelligent Transportation Systems Conference (ITSC)*, pages 1283–1289, 2019. 2
- [4] Daniele Cattaneo, Domenico Giorgio Sorrenti, and Abhinav Valada. Cmrnet++: Map and camera agnostic monocular visual localization in lidar maps. *IEEE International Conference on Robotics and Automation (ICRA) Workshop on Emerging Learning and Algorithmic Methods for Data Association in Robotics*, 2020. 2
- [5] Jen-Hao Rick Chang, Wei-Yu Chen, Anurag Ranjan, Kwang Moo Yi, and Oncel Tuzel. Pointersect: Neural rendering with cloud-ray intersection. In *CVPR*, 2023. 1
- [6] Peng Dai, Yinda Zhang, Zhuwen Li, Shuaicheng Liu, and Bing Zeng. Neural point cloud rendering via multi-plane projection. In *Proceedings of the IEEE/CVF Conference on Computer Vision and Pattern Recognition*, pages 7830–7839, 2020. 1
- [7] Mengdan Feng, Sixing Hu, Marcelo H Ang, and Gim Hee Lee. 2D3D-Matchnet: Learning To Match Keypoints Across 2D Image And 3D Point Cloud. In *2019 International Conference on Robotics and Automation (ICRA)*, pages 4790–4796, 2019. ISSN: 2577-087X. 2
- [8] Martin A. Fischler and Robert C. Bolles. Random sample consensus: a paradigm for model fitting with applications to image analysis and automated cartography. *Communications of the ACM*, 24(6):381–395, 1981. 4, 5
- [9] S. Garrido-Jurado, R. Muñoz-Salinas, F.J. Madrid-Cuevas, and M.J. Marín-Jiménez. Automatic generation and detection of highly reliable fiducial markers under occlusion. *Pattern Recognition*, 47(6):2280–2292, 2014. 1
- [10] Michael Grupp. evo: Python package for the evaluation of odometry and slam. <https://github.com/MichaelGrupp/evo>, 2017. 7
- [11] Tao Hu, Xiaogang Xu, Shu Liu, and Jiaya Jia. Point2pix: Photo-realistic point cloud rendering via neural radiance fields. In *Proceedings - 2023 IEEE/CVF Conference on Computer Vision and Pattern Recognition, CVPR 2023*, pages 8349–8358. IEEE Computer Society, 2023. 1
- [12] Youngji Kim, Jinyong Jeong, and Ayoung Kim. Stereo Camera Localization in 3D LiDAR Maps. In *2018 IEEE/RSJ International Conference on Intelligent Robots and Systems (IROS)*, pages 1–9, 2018. ISSN: 2153-0866. 2
- [13] Jianghao Leng, Chao Sun, Bo Wang, Yungang Lan, Zhishuai Huang, Qinyan Zhou, Jiahao Liu, and Jiajun Li. Cross-Modal LiDAR-Visual-Inertial Localization in Prebuilt LiDAR Point Cloud Map Through Direct Projection. *IEEE Sensors Journal*, 24(20):33022–33035, 2024. 1
- [14] Vincent Lepetit, Francesc Moreno-Noguer, and Pascal Fua. EPnP: An Accurate O(n) Solution to the PnP Problem. *International Journal of Computer Vision*, 81(2):155–166, 2009. 2, 4, 5, 1
- [15] Jiaxin Li and Gim Hee Lee. DeepI2P: Image-to-Point Cloud Registration via Deep Classification. pages 15960–15969, 2021. 2
- [16] Minhao Li, Zheng Qin, Zhirui Gao, Renjiao Yi, Chenyang Zhu, Yulan Guo, and Kai Xu. 2D3D-MATR: 2D-3D Matching Transformer for Detection-free Registration between Images and Point Clouds. In *2023 IEEE/CVF International Conference on Computer Vision (ICCV)*, pages 14082–14092, 2023. ISSN: 2380-7504. 2
- [17] Jianheng Liu, Chunran Zheng, Yunfei Wan, Bowen Wang, Yixi Cai, and Fu Zhang. Neural surface reconstruction and rendering for lidar-visual systems, 2024. 2
- [18] D.G. Lowe. Object recognition from local scale-invariant features. In *Proceedings of the Seventh IEEE International Conference on Computer Vision*, pages 1150–1157 vol.2, Kerkyra, Greece, 1999. IEEE. 2
- [19] Nick Michiels, Lode Jorissen, Jeroen Put, Jori Liesenborgs, Ishtar Vandebroek, Eric Joris, and Frank Van Reeth. Tracking and co-location of global point clouds for large-area indoor environments. *Virtual Reality*, 28(2):106, 2024. 2
- [20] Steven Moonen, Bram Vanherle, Joris de Hoog, Taoufik Bourgana, Abdellatif Bey-Temsamani, and Nick Michiels. Cad2render: A modular toolkit for gpu-accelerated photorealistic synthetic data generation for the manufacturing industry. In *2023 IEEE/CVF Winter Conference on Applications of Computer Vision Workshops (WACVW)*, pages 583–592, 2023. 2
- [21] Juncheng Mu, Chengwei Ren, Weixiang Zhang, Liang Pan, Xiao-Ping Zhang, and Yue Gao. Diff2i2p: Differentiable image-to-point cloud registration with diffusion prior. In *Proceedings of the IEEE/CVF International Conference on Computer Vision (ICCV)*, pages 25777–25787, 2025. 2
- [22] Raul Mur-Artal and Juan D. Tardós. Fast relocalisation and loop closing in keyframe-based SLAM. In *2014 IEEE International Conference on Robotics and Automation (ICRA)*, pages 846–853, 2014. ISSN: 1050-4729. 1, 4
- [23] Rafael Muñoz-Salinas, Jianheng Liu, Francisco J. Romero-Ramirez, Manuel J. Marín-Jiménez, and Fu Zhang. LiDAR as a Geometric Prior: Enhancing Camera Pose Tracking Through High-Fidelity View Synthesis. *Applied Sciences*, 15(15):8743, 2025. Publisher: Multidisciplinary Digital Publishing Institute. 2

- [24] Quang-Hieu Pham, Mikaela Angelina Uy, Binh-Son Hua, Duc Thanh Nguyen, Gemma Roig, and Sai-Kit Yeung. LCD: Learned cross-domain descriptors for 2D-3D matching. In *AAAI Conference on Artificial Intelligence*, 2020. 2
- [25] Guilherme Potje, Felipe Cadar, André Araujo, Renato Martins, and Erickson R. Nascimento. Xfeat: Accelerated features for lightweight image matching. In *Proceedings of the IEEE/CVF Conference on Computer Vision and Pattern Recognition (CVPR)*, pages 2682–2691, 2024. 4
- [26] Ruslan Rakhimov, Andrei-Timotei Ardelean, Victor Lepitskiy, and Evgeny Burnaev. Npbg++: Accelerating neural point-based graphics. In *Proceedings of the IEEE/CVF Conference on Computer Vision and Pattern Recognition (CVPR)*, pages 15969–15979, 2022. 1
- [27] Siyu Ren, Yiming Zeng, Junhui Hou, and Xiaodong Chen. CorrI2P: Deep Image-to-Point Cloud Registration via Dense Correspondence. *IEEE Transactions on Circuits and Systems for Video Technology*, 33(3):1198–1208, 2023. Conference Name: IEEE Transactions on Circuits and Systems for Video Technology. 2
- [28] Olaf Ronneberger, Philipp Fischer, and Thomas Brox. U-Net: Convolutional Networks for Biomedical Image Segmentation. In *Medical Image Computing and Computer-Assisted Intervention – MICCAI 2015*, pages 234–241, Cham, 2015. Springer International Publishing. 3
- [29] Ethan Rublee, Vincent Rabaud, Kurt Konolige, and Gary Bradski. ORB: An efficient alternative to SIFT or SURF. In *2011 International Conference on Computer Vision*, pages 2564–2571, 2011. ISSN: 2380-7504. 4
- [30] Johannes Lutz Schönberger and Jan-Michael Frahm. Structure-from-motion revisited. In *Conference on Computer Vision and Pattern Recognition (CVPR)*, 2016. 2, 6
- [31] Markus Schütz, Bernhard Kerbl, and Michael Wimmer. Rendering point clouds with compute shaders and vertex order optimization. *Computer Graphics Forum*, 40(4):12, 2021. 3
- [32] Shubham Singh, Yash Sharma, Amer Liaqat, and Roy S. Kalawsky. Evaluation of XR device’s real-world tracking accuracy and depth perception from an industrial point of view. *Virtual Reality*, 29(3):118, 2025. 1
- [33] Shinya Sumikura, Mikiya Shibuya, and Ken Sakurada. OpenVSLAM: A Versatile Visual SLAM Framework. In *Proceedings of the 27th ACM International Conference on Multimedia*, pages 2292–2295, New York, NY, USA, 2019. ACM. 5, 6
- [34] S. Umeyama. Least-squares estimation of transformation parameters between two point patterns. *IEEE Transactions on Pattern Analysis and Machine Intelligence*, 13(4):376–380, 1991. 7
- [35] Joni VANHERCK, Brent Zoomers, Tom Mertens, Lode Jorissen, and Nick Michiels. Real-time Neural Rendering of LiDAR Point Clouds. In *Eurographics 2025 - Short Papers*. The Eurographics Association, 2025. 1, 3
- [36] Bing Wang, Changhao Chen, Zhaopeng Cui, Jie Qin, Chris Xiaoxuan Lu, Zhengdi Yu, Peijun Zhao, Zhen Dong, Fan Zhu, Niki Trigoni, and Andrew Markham. P2-Net: Joint Description and Detection of Local Features for Pixel and Point Matching. In *2021 IEEE/CVF International Conference on Computer Vision (ICCV)*, pages 15984–15993, 2021. 2
- [37] Haiping Wang, Yuan Liu, Bing Wang, Yujing Sun, Zhen Dong, Wenping Wang, and Bisheng Yang. Freereg: Image-to-point cloud registration leveraging pretrained diffusion models and monocular depth estimators. In *ICLR*, 2024. 2
- [38] Zhou Wang, A.C. Bovik, H.R. Sheikh, and E.P. Simoncelli. Image quality assessment: from error visibility to structural similarity. *IEEE Transactions on Image Processing*, 13(4): 600–612, 2004. 6
- [39] Chandan Yeshwanth, Yueh-Cheng Liu, Matthias Nießner, and Angela Dai. Scannet++: A high-fidelity dataset of 3d indoor scenes. In *Proceedings of the International Conference on Computer Vision (ICCV)*, 2023. 2, 6
- [40] Huai Yu, Weikun Zhen, Wen Yang, Ji Zhang, and Sebastian Scherer. Monocular Camera Localization in Prior LiDAR Maps with 2D-3D Line Correspondences. In *2020 IEEE/RSJ International Conference on Intelligent Robots and Systems (IROS)*, pages 4588–4594, Las Vegas, NV, USA, 2020. IEEE. 2
- [41] Chunran Zheng, Wei Xu, Zuhao Zou, Tong Hua, Chongjian Yuan, Dongjiao He, Bingyang Zhou, Zheng Liu, Jiarong Lin, Fangcheng Zhu, Yunfan Ren, Rong Wang, Fanle Meng, and Fu Zhang. FAST-LIVO2: Fast, Direct LiDAR-Inertial-Visual Odometry. *IEEE Transactions on Robotics*, 41:326–346, 2025. 1
- [42] Jianhao Zheng, Zihan Zhu, Valentin Bieri, Marc Pollefeys, Songyou Peng, and Iro Armeni. Wildgslam: Monocular gaussian splatting slam in dynamic environments. In *Proceedings of the IEEE/CVF Conference on Computer Vision and Pattern Recognition (CVPR)*, pages 11461–11471, 2025. 1
- [43] Yu Zhong. *Intrinsic shape signatures: A shape descriptor for 3D object recognition*. 2009. Journal Abbreviation: IEEE International Conference on Computer Vision Workshops Pages: 696 Publication Title: IEEE International Conference on Computer Vision Workshops. 2

CRISTAL: Real-time Camera Registration in Static LiDAR Scans using Neural Rendering

Supplementary Material

6. Custom Dataset Acquisition

To evaluate our methods, we created two ground-truth datasets:

- **Lab dataset:** a real-world dataset using a sub-millimeter accurate motion capture system and a static LiDAR scanner,
- **Synthetic dataset:** a dataset simulating a static LiDAR scanner and video trajectories in Unity.

In the following sections, we explain the acquisition of each dataset in more detail.

6.1. Lab Dataset

We captured this dataset using a Leica RTC360 static LiDAR scanner and a Qualisys motion capture system as the ground-truth reference. The point cloud contains 71 M points and covers an area of approximately 6×6 m. According to the datasheet, the Leica RTC360 achieves an accuracy of 1.9 mm deviation at 10 m from the scanner. The motion capture setup includes three Arqus cameras and eight Miquis cameras, recording ground-truth data at 300 Hz. Videos were captured with an Intel RealSense D455 camera (shown in Fig. 5a) with a resolution of 1280×720 at 30 fps. A rigid marker structure was attached to the camera for tracking with the motion capture system. Figure 6 shows the captured environment. An overview of each sequence is given by Tab. 4.

Sequence	#Frames	Length (m)
lab_1	4496	64.1
lab_2	4433	36.1
lab_3	4468	41.7

Table 4. Overview of the captured sequences in the Lab dataset. ‘#Frames’ shows the number of frames in the sequence, and ‘Length’ shows the length of the trajectory in meters.

Following [42], we synchronized the camera and motion capture system using an infrared light visible to both at the start of each sequence. The light was toggled several times, producing corresponding timestamps used to compute the temporal offset between the systems and derive a ground-truth pose for each camera frame.

To determine the offset between the camera’s optical center and the attached markers, we positioned the camera with its markers stationary and aimed it at several reference markers (see Fig. 5b). In the camera image, we extracted

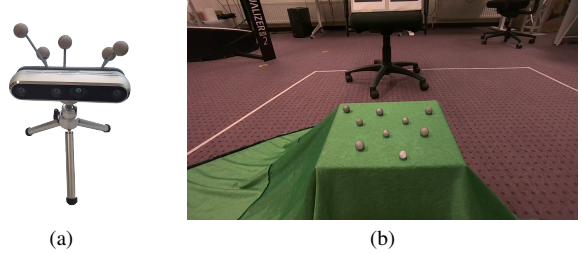


Figure 5. (a) Intel RealSense D455 setup with attached markers (rigid body) to capture the sequences. (b) Calibration image to determine the offset between the rigid body origin and the optical center of the camera.

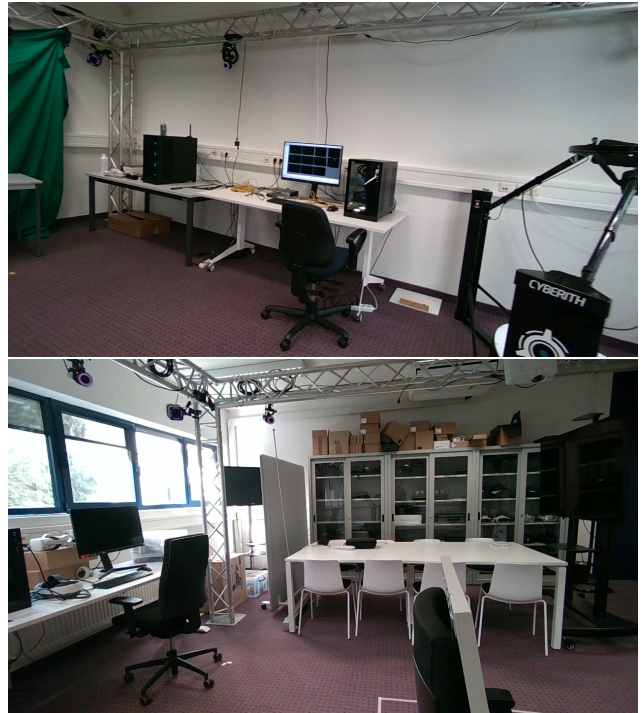


Figure 6. Lab environment with the Qualisys motion capture system.

the center of each marker to obtain their 2D coordinates. The markers were placed on a green background to facilitate segmentation. Their 3D positions were obtained from Qualisys, providing 2D–3D correspondences between the Qualisys coordinate system and the camera image. We then computed the camera pose relative to the Qualisys system using PnP [14]. Because the rigid body’s pose is also known

in Qualisys coordinates, we determined the offset from the camera’s optical center to the rigid body origin. We applied it to all Qualisys ground-truth measurements to obtain the final ground-truth camera poses.

6.2. Synthetic Dataset

We generated the synthetic dataset using the Unity game engine. The synthetic data generation pipeline CAD2Render [20] was extended to support capturing multiple point clouds, similar to a static LiDAR scanner. This is done in two stages. First, color information is captured from the LiDAR position by rendering six images with a 90° field of view in all cardinal directions to form a cubemap. Second, the world position coordinates of the visible points are captured using the RTX ray tracing pipeline, which enables the same sampling pattern as a physical LiDAR scanner. While raytracing the world positions, the ray direction is also used to sample the cubemap and assign color to each 3D point. Scanner positions in the scene were manually selected to replicate realistic scanning strategies. We captured a large industrial warehouse covering $\sim 60 \times 40$ m as a synthetic dataset, which can be seen in Fig. 7. The point cloud contains 262 M points, the videos were recorded with a resolution of 1280×720 at 30 fps. Table 5 gives an overview of each sequence. Given this is a synthetic dataset, there are no synchronization issues between the camera and the pose, and the ground-truth pose for each camera frame can be easily extracted directly from Unity.



Figure 7. Synthetic dataset: an industrial warehouse in Unity.

Seq.	#Frames	Length (m)
synth_1	2075	136
synth_2	1899	134.2
synth_3	1585	99.3

Table 5. Overview of the captured sequences in the Synthetic dataset. ‘#Frames’ shows the number of frames in the sequence, and ‘Length’ shows the length of the trajectory in meters.

7. Additional experiments

We show additional qualitative results on the ScanNet++ dataset in Fig. 8 and Fig. 9. These examples show rendered views from the estimated camera pose overlaid with real camera images, ghosting or blur indicates pose misalignment. Our methods clearly show improved alignment compared to the poses provided by ScanNet++.

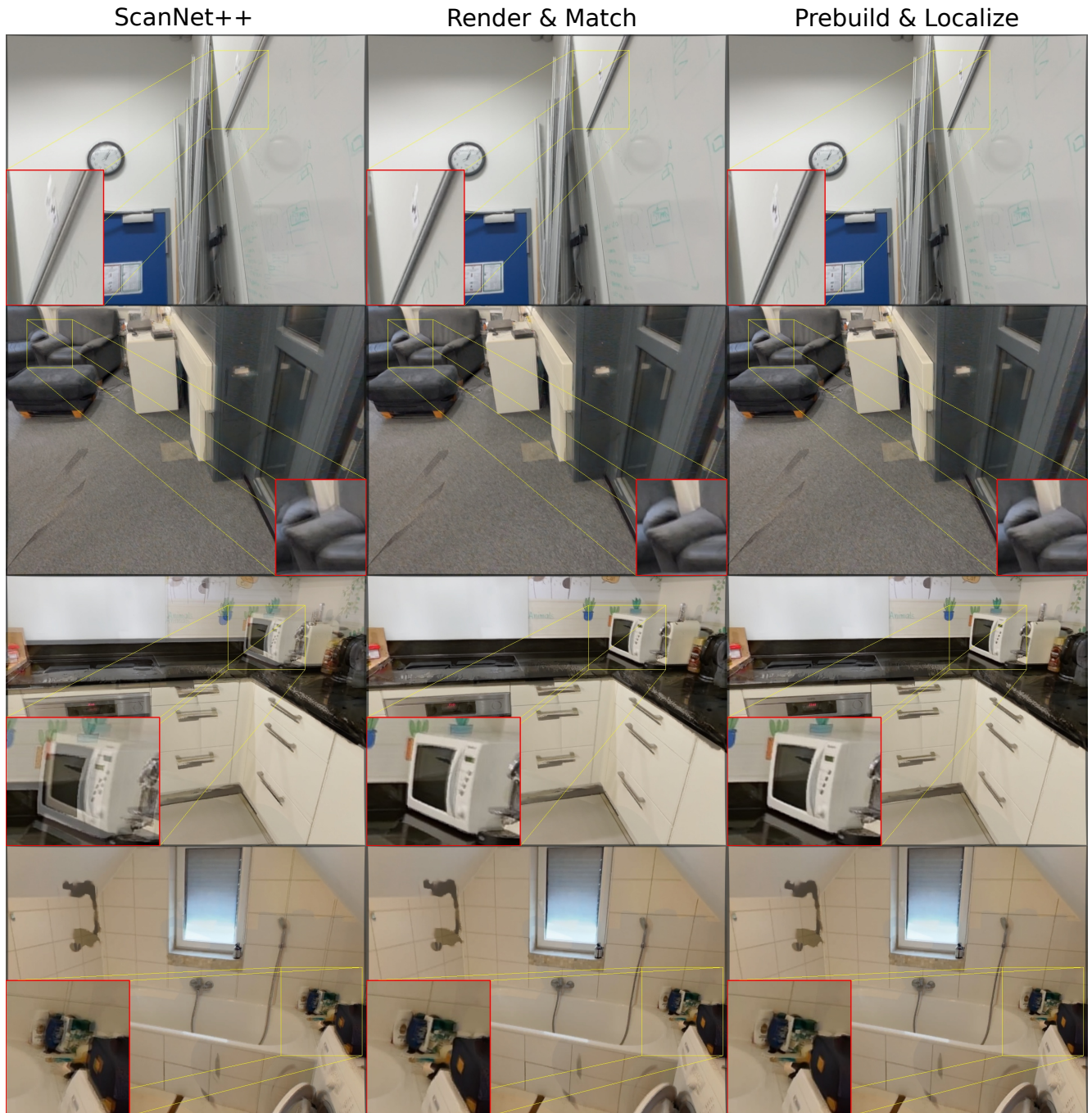


Figure 8. Each image displays an overlay of the target camera frame and a neural rendering of the point cloud generated from the estimated camera pose. We show results for ScanNet++, the Render & Match approach, and the Prebuild & Localize method. Misalignment, visible as ghosting or blur, suggests pose estimation errors.

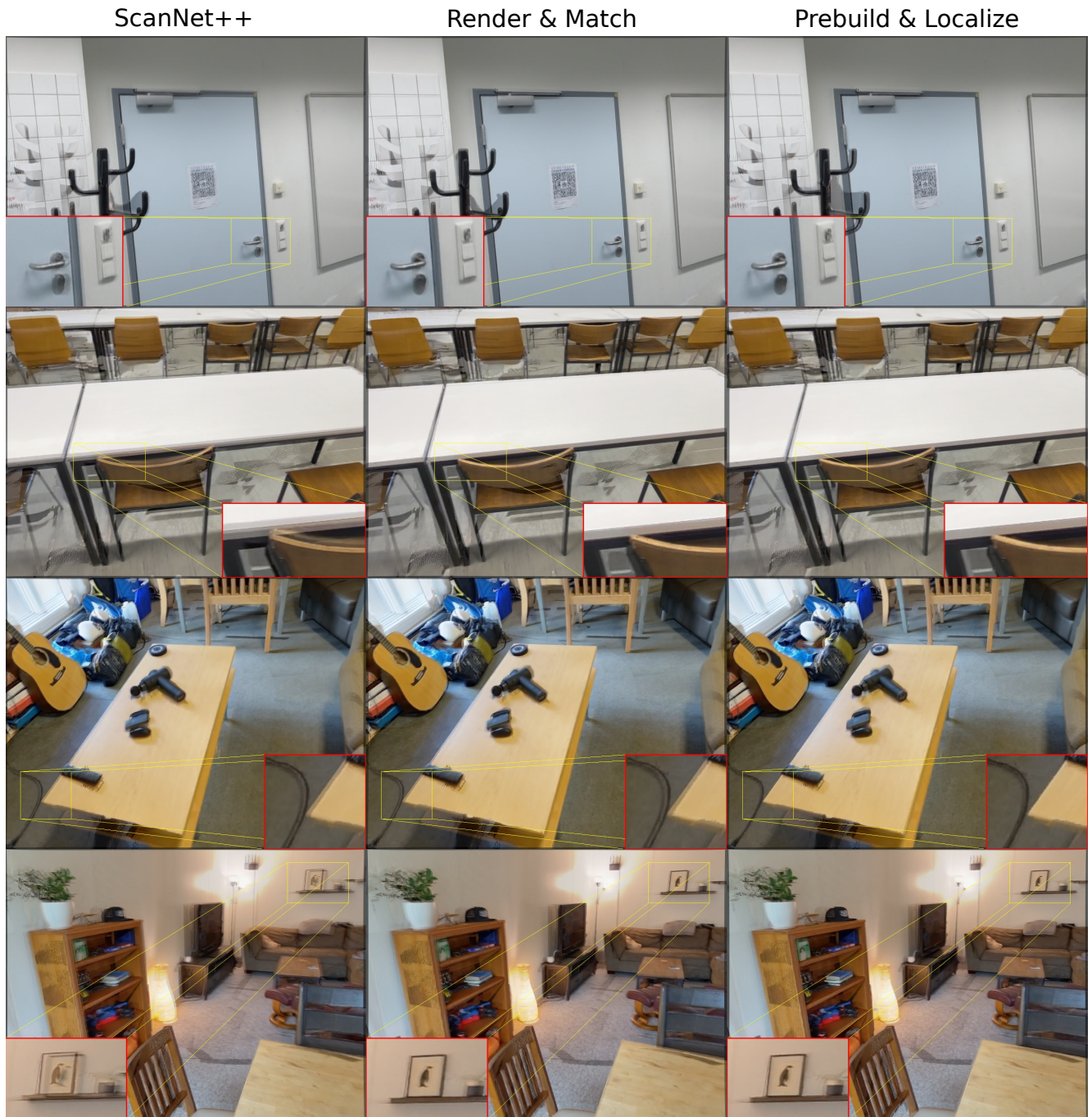


Figure 9. Each image displays an overlay of the target camera frame and a neural rendering of the point cloud generated from the estimated camera pose. We show results for ScanNet++, the Render & Match approach, and the Prebuild & Localize method. Misalignment, visible as ghosting or blur, suggests pose estimation errors.